Simulation of Transverse Gaseous Injection Through Diamond Ports into Supersonic Freestream

Ravichandra Srinivasan* and Rodney D. W. Bowersox†
Texas A&M University, College Station, Texas 77843

Numerical simulations were performed to study the secondary flow structures induced by transverse underexpanded sonic injection through diamond-shaped orifices in a supersonic ($M = 2.0$ and 5.0) crossflow. Two new vortex features were observed in the vicinity of the injector port when compared to circular injector ports. The first pair, which has the potential to serve as a mixing enhancement mechanism, was located near the leading edge of the injector. The second pair was located just downstream of the barrel shock. This gasdynamically induced flow structure, termed the lateral counter-rotating vortex pair, has the potential to act as a flame-holding device. It was observed that the lateral counter-rotating vortex pair did not form in simulations of angled transverse injection. However, the leading-edge vortex pair was found to be stronger in angled injection simulations. To combine the advantages of the leading-edge mixing and the lateral counter-rotating vortex pair structure, additional numerical simulations were performed with 27.5–90 deg and 45–90 deg hybrid injectors. The lateral counter-rotating vortex pair structure was observed in both of these simulations along with enhanced leading-edge mixing as compared to the normal injection case.

Nomenclature

d_{eff}	=	injector throat diameter ($=4.89$ mm)
J	=	jet to freestream momentum flux ratio, $\rho_j u_j^2 / \rho_\infty u_\infty^2$
J_{eff}	=	$J \sin(\alpha)$
k	=	turbulent kinetic energy
M	=	Mach number
p	=	pressure, N/m^2
T	=	temperature, K
x	=	axial coordinate
y	=	transverse coordinate
z	=	lateral coordinate
α	=	incidence angle of injector leading edge relative to x axis, positive counterclockwise
β	=	incidence angle of injector trailing edge relative to x axis, positive counterclockwise
γ	=	injector orifice half-angle
δ	=	boundary layer thickness
μ	=	viscosity
ρ	=	density, kg/m^3

Subscripts

j	=	injector
t	=	turbulent quantity
0	=	stagnation condition
2	=	downstream of a shock wave
∞	=	freestream condition

I. Introduction

EFFICIENT fuel injection is one of the key challenges in the development of scramjets for the purpose of powering atmospheric hypersonic flight. Airflow in a scramjet is characterized by extremely short residence times [1], on the order of a few milliseconds. The injection, mixing, and combustion processes have to be completed within these residence times. Enhanced fuel–air mixing is required for efficient fuel consumption and power generation. Also, to increase thrust, induced drag in the combustor has to be minimized. Thus there is a requirement for optimized fuel injector designs with the ability to address all of these issues. The current leading candidate for flame holding within scramjets is the wall cavity flame concept [2,3]. Although this concept has proven effective, the cavity induces unsteadiness in the flowfield, and it has to endure a very harsh environment.

Transverse jets have also been used as reaction control jets for maneuvering high-speed aircraft [4–6]. The use of these jets alleviates some of the problems associated with aerodynamic surfaces. The surface pressure distribution around the injector port affects the performance of the jet as a control element. This in turn is dependent on numerous factors including the strength of the interaction shock and the structure of the fluid exiting the injector port.

The flowfield generated by a transverse underexpanded jet exiting normally into a supersonic freestream has been thoroughly explored in various studies [7–9]. The injector fluid obstructs the freestream flow leading to the formation of an interaction shock upstream of the injector port. A separation region is also created in the boundary layer upstream of the injector in situations where δ/d is $\mathcal{O}(1)$ [8]. The separation region creates a weak lambda-shaped shock that merges with the interaction shock. The jet expands to an effective backpressure as it exits into the freestream. In the case of circular injector ports, this expansion terminates in a barrel-shaped shock and a Mach disk. The upstream separation region creates a horseshoe-shaped vortex that wraps around the injector exit along the wall. Interaction between the freestream and the injector fluid around the port leads to the formation of an axial counter-rotating vortex pair (CVP) in the plume region. A shear layer develops downstream of the injector due to the action of freestream fluid on the jet plume. Vortices are also formed in the wake region behind the injector.

Angled injection is a means of reducing the total pressure loss associated with the strong bow shock. Further, low-angled injection has been shown to create a measurable increase in the overall combustion thrust potential [10] as compared to normal injection. For both angled and normal injection, the penetration was found to be directly proportional to the momentum flux ratio.

Wedge-shaped injectors with circular trailing edges have been investigated and the results show that this geometry leads to better performance as compared to circular injectors [11]. Injection into a supersonic flow using diamond-shaped injectors has been

Fig. 1 Coordinate system and test section (mm).

Fig. 2 Injector configuration (mm).
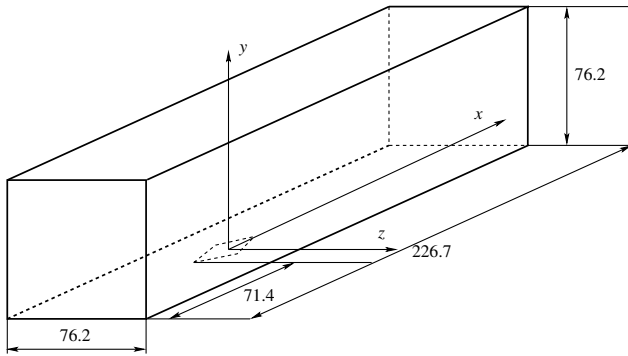
investigated using experimental techniques [12,13]. It was found that the strength of the interaction shock decreases due to the streamlined nature of the diamond shape of the injector exit [12]. This leads to lower total pressure loss downstream of the injector. The penetration was higher at lower momentum flux ratios for diamond injectors as compared to circular and wedge-shaped injectors [13]. The effects of sweeping the diamond injector in the downstream direction was found to increase penetration, similar to the observations made in the case of circular injectors.

The objective of this research was to numerically study the effects of the injector barrel shock, induced by transverse underexpanded sonic injection through diamond-shaped orifices, on the secondary flow structures in a supersonic flow. Specifically, the role of the diamond-shaped injector in the formation of the barrel shock and the near-field flow structures were examined. Numerical results were validated against experimental data for the normal injection case.

II. Research Approach

A. Geometry

The domain used in the normal injection simulation was that of experiments conducted by Bowersox et al. [12]. Figure 1 is an illustration of the coordinate system and test section. Freestream conditions are listed in Table 1. The injector fluid was air in all the test cases. For all of the flows where the freestream Mach number was 5.0, the diamond injector port had a half-angle of 15 deg (see Fig. 2, $\gamma = 15$ deg). This half-angle was chosen with the goals of 1) a weak leading-edge shock and 2) minimization of tunnel wall reflections. The injector port had an area of 18.8 mm^2 with an effective diameter of 4.89 mm. The leading- and trailing-edge sweep angles of the injector port are denoted in Fig. 2 by α and β, respectively. Normal injection simulations were performed by setting both the leading- and trailing-edge sweep angles to 90 deg and for the angled injection simulation, these angles were set to 45 deg. The leading edge of the injector was located 71.4 mm downstream of the test section inlet. The total pressure of the injectant was 0.10 MPa and the total temperature was 295.0 K. The exit Mach number of the jet was approximately 1.0. Numerical simulations were also performed at the Mach 5.0 freestream condition using hybrid injectors with leading-edge angles (α) of 27.5 and 45 deg and a trailing-edge angle (β) of 90 deg. The exit area of these injectors was the same as that of the normal injector. The injector inlet area for the hybrid injectors was increased to 56.4 mm^2 to accommodate the decreased injection angle.

Simulations were also performed at the Mach 2.0 freestream conditions listed in Table 1. These simulations had the same static pressure and temperature conditions as the Mach 5.0 cases. The jet
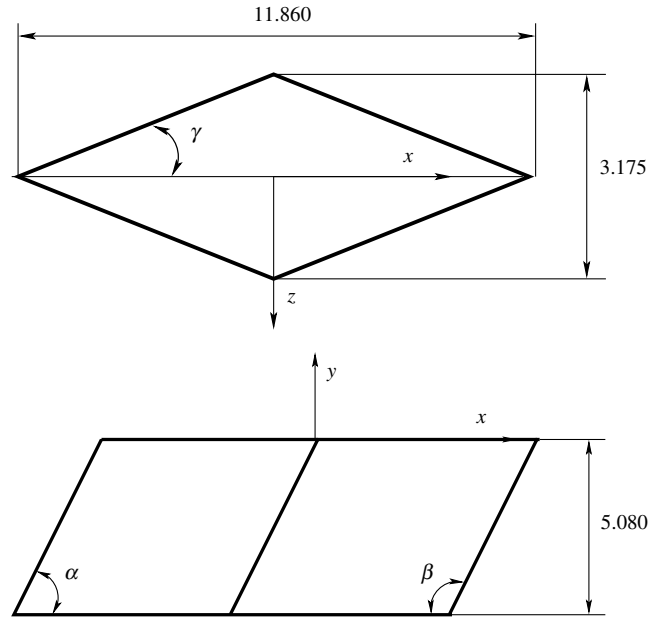
fluid was injected at 90 deg to the freestream through diamond ports with half-angles of 15 and 10 deg. The cross-sectional area of the 10 deg injector was equal to that of the 15 deg injector. The length of the injector port in the freestream direction was increased to compensate for the reduction in injector half-angle.

B. Grid Generation

The flow domain was discretized into a structured grid using the Gridgen (Pointwise, Inc.) software package. Flow symmetry was assumed on the xy plane along the tunnel centerline (see Fig. 3). The discretized domain height was limited to $y/d_{\mathrm{eff}} = 7.78$ since the flow structures of interest were within this distance from the tunnel floor. The modeled domain includes the injector port to include flow losses within the port. The grid was composed of two blocks, one each for the tunnel and the injector with a total of approximately 5.4×10^6 cells. Grid points were clustered around the injector port and in the plume and wake region as shown in Fig. 3. Clustering was also performed in the boundary layer to ensure a $y^+ < 1$ at the first grid point away from the wall. Grid convergence was performed in situ using the sequencing procedure provided in the flow solver (convergence is discussed in Sec. III).

C. Boundary Conditions

Freestream conditions are specified at the inlet of the domain with a boundary layer whose thickness (8.3 mm) matches that observed in the Mach 5.0 experiments. Symmetry is specified on the xy plane along the tunnel centerline. Extrapolation conditions are specified on top and exit surfaces. Adiabatic no-slip conditions were applied at the tunnel floor and injector port wall. Tangency boundary conditions were applied at the tunnel sidewalls. Mach number, static pressure, and density were specified at the injector inlet. The injector inlet boundary conditions for the normal injection low and high pressure cases are listed in Table 2. Also listed are the conditions for the hybrid injectors.

D. Flow Solver

Aerosoft Inc.'s General Aerodynamics Simulation Program (GASP) [14] was used for all two-equation simulations related to this work. GASP is an established computational fluid dynamics (CFD) solver that has been evolving since its commercial release in 1994. Over that time, it has been shown to reliably simulate a wide variety of flows that include both wall-bounded and free-shear flows [15].

For the present study GASP was set up to simulate the Favre averaged conservation law equations. Turbulence was modeled
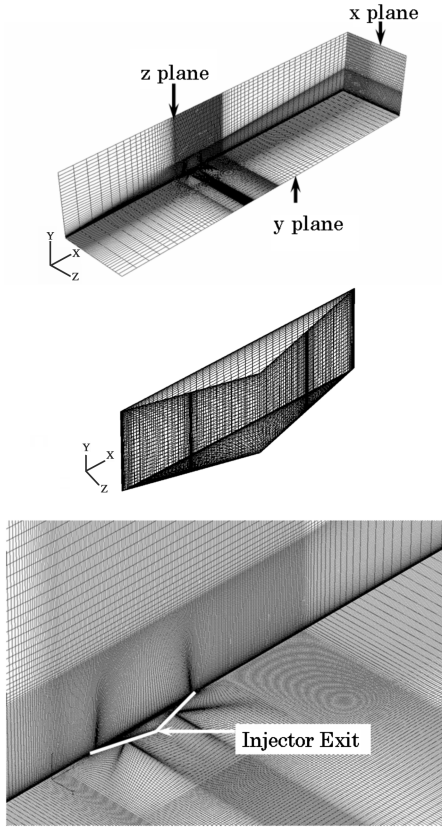
Table 1 Freestream conditions

Mach	p_0, MPa	T_0, K	$Re/\mathrm{m}, \times 10^6$	δ, mm
5.0	2.40	360.0	53.0	8.3
2.0	0.38	108.5	21.0	8.3

Fig. 3 Structured grid for normal injection.

The model equation for the specific dissipation rate ω is

$$\frac{\partial \rho \omega}{\partial t} + \frac{\partial (\rho u \omega)}{\partial x} + \frac{\partial (\rho v \omega)}{\partial y} + \frac{\partial (\rho w \omega)}{\partial z} = \frac{\partial \tau_x^\omega}{\partial x} + \frac{\partial \tau_y^\omega}{\partial y} + \frac{\partial \tau_z^\omega}{\partial z}$$
$$+ C_{P_\omega} \left[\mu_t S^2 - \frac{2}{3} \rho K (\nabla \cdot \mathbf{V}) \right] \left(\frac{\omega}{K} \right) - C_{D_\omega} \rho \varepsilon \frac{\omega}{K} \quad (4)$$

The viscous terms are given by

$$\tau_{x_i}^\omega = \left(\mu + \frac{\mu_t}{Pr_\omega} \right) \frac{\partial \omega}{\partial x_i} \quad (5)$$

The eddy viscosity is evaluated using

$$\mu_t = C_\mu \rho k / \omega \quad (6)$$

The parameters used for closure of Eqs. (1) and (4) are given by

$$C_{P_K} = 1.0 \qquad C_{P_\omega} = 5/9 \qquad C_{D_K} = 1.0 \qquad C_{D_\omega} = 5/9$$
$$Pr_K = 2.0 \qquad Pr_\omega = 2.0 \qquad C_\mu = 0.09 \quad (7)$$

E. Simulation Procedure

GASP uses structured grids to perform fluid flow simulations. A grid file representing the flow domain in PLOT3D format was imported into GASP. Grid surfaces were grouped based on boundary conditions discussed in the previous section. The grid was sequenced to obtain solutions on coarse and medium grids. Inviscid fluxes were evaluated using third-order upwinding and the Roe approximate Riemann solver [17] with Harten's entropy correction [18]. The minimum modulus [19] method was used to limit solution variables near discontinuities. Turbulence was simulated using the two-equation k–ω (1998) model [16]. Solutions from coarse and medium grids were interpolated to the next finer sequence by the flow solver to speed up solution convergence and verify grid convergence. Initial iterations on all grid levels were executed with a local Courant–Friedrichs–Lewy (CFL) number. Remaining iterations were executed using the global CFL number.

III. Numerical Convergence and Validation

First, the numerical convergence results are presented. Second, the numerical results are compared to experiment to assess the solution accuracy. The 90 deg (case 1) diamond injector was used as the testbed for these assessments.

A. Grid and Solution Convergence

For all the simulations presented here, the residual (L_2 norm) was reduced by at least 5 orders of magnitude. It was observed that there was no change in the residual value after about 500 iterations. However, the surface properties required additional iterations to achieve steady state. This was monitored using the surface pressure values along the centerline of the tunnel floor. Pressure values along the tunnel floor centerline were output from the solver at every 100th

using the k–ω [16] two-equation model. More specifically, the integral form of the governing equations for a single species gas was solved.

The turbulent kinetic energy equation in the k–ω turbulence model used is

$$\frac{\partial \rho K}{\partial t} + \frac{\partial (\rho u K)}{\partial x} + \frac{\partial (\rho v K)}{\partial y} + \frac{\partial (\rho w K)}{\partial z} = \frac{\partial \tau_x^K}{\partial x} + \frac{\partial \tau_y^K}{\partial y} + \frac{\partial \tau_z^K}{\partial z}$$
$$+ C_{P_K} \left[\mu_t S^2 - \frac{2}{3} \rho K (\nabla \cdot \mathbf{V}) \right] - C_{D_K} \rho \varepsilon \quad (1)$$

The viscous terms are given by

$$\tau_{x_i}^K = \left(\mu + \frac{\mu_t}{Pr_K} \right) \frac{\partial K}{\partial x_i} \quad (2)$$

and the strain invariant S^2 is

$$S^2 = (u_{i,j} + u_{j,i}) u_{i,j} - \frac{2}{3} u_{k,k}^2 \quad (3)$$

Table 2 Jet conditions

| Case | Half-angle, γ | Injection angle | | J | M_j | p, MPa | ρ, kg/m^3 | M_∞ |
		α	β					
1	15 deg	90 deg	90 deg	0.4	1.0	0.052	0.7771	5.0
2	15 deg	90 deg	90 deg	2.1	1.0	0.254	3.6856	5.0
3	15 deg	45 deg	45 deg	0.4	1.0	0.052	0.7771	5.0
4	15 deg	27.5 deg	90 deg	0.4	1.0	0.098	1.1996	5.0
5	15 deg	45 deg	90 deg	0.4	1.0	0.098	1.1996	5.0
6	15 deg	90 deg	90 deg	2.7	1.0	0.052	0.7771	2.0
7	10 deg	90 deg	90 deg	2.7	1.0	0.052	0.7771	2.0
8	10 deg	90 deg	90 deg	0.4	1.0	0.052	0.7771	5.0
9	20 deg	90 deg	90 deg	0.4	1.0	0.052	0.7771	5.0
10	15 deg	27.5 deg	27.5 deg	0.4	1.0	0.052	0.7771	5.0
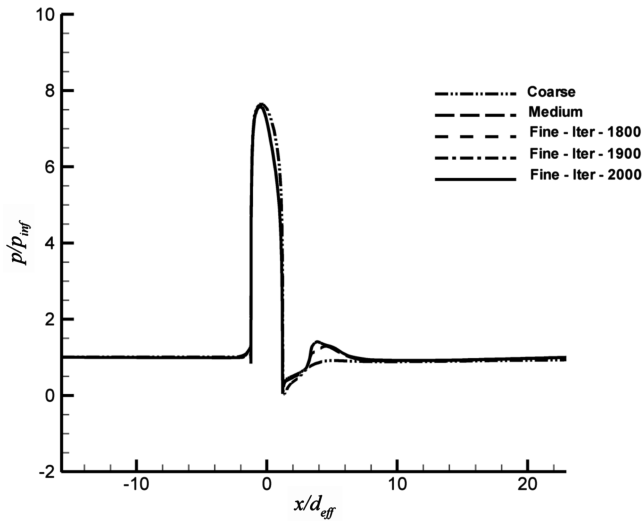
Fig. 4   Grid and solution convergence plot showing normalized surface pressure along the centerline of the tunnel floor.
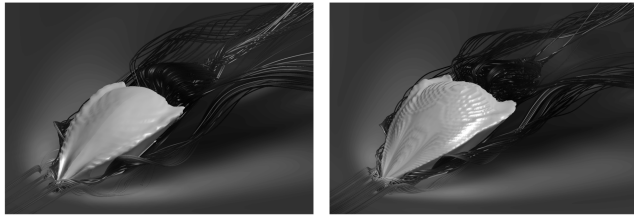
a) Medium grid   b) Fine grid

Fig. 5   Flow structures obtained using medium and fine grids. Refer to Fig. 10 for surface pressure contour levels.

iteration. A plot of the pressure on the tunnel centerline is shown in Fig. 4, indicating solution convergence. The secondary flow structures found in the fine grid were also observed in the medium grid as shown in Fig. 5.

The grid sequencing option in GASP was used to ensure that the solution obtained was grid converged. From the initial (fine) grid input into GASP, two additional grid levels were generated. The medium grid was obtained by eliminating every second point in the fine grid and the coarse grid was obtained by eliminating every second point in the medium grid. Solutions were then generated for the coarse, medium, and fine grids. A plot of pressure along the centerline of the tunnel floor is shown for the three grid levels in Fig. 4. The pressure plots for the medium and fine grids coincide, indicating that grid convergence has been achieved.

B.   Comparison with Experimental Data

Numerical and experimental [12] surface oil flow visualizations for case 1 (Table 2) are shown in Fig. 6. The experimental result is annotated indicating the salient flow features. The freestream flow is from left to right. The shock-induced separation region is the lighter
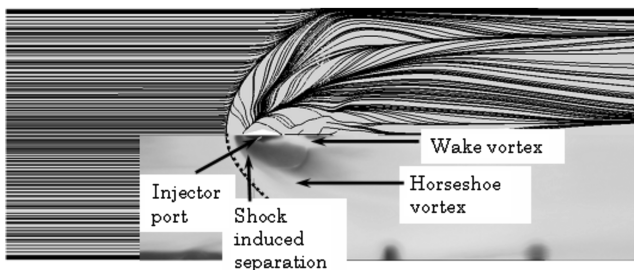

Fig. 6   Surface oil flow comparison between experimental and numerical results, case 1.

region ahead of the interaction shock. This region is difficult to discern in the printed image. Hence, a dashed line is drawn to show the onset of the separation region. This is similar to that seen in results obtained from GASP. The horseshoe vortex can be observed in the images as it wraps around the injector. The distance separating the two arms of the vortex is correctly predicted by the Reynolds-averaged Navier–Stokes equations (RANS) model. Starting at the trailing edge of the injector port is a pair of wake vortices clearly seen in experimental results. Although not clearly visible in numerical oil flow results, the presence of these wake vortices can be observed in the streamlines and cross-sectional velocity vectors as discussed later in this section. The dark region between the wake vortices close to the injector is the location of a peak pressure area on the tunnel floor. In summary, the predicted size and location of the surface oil flow features were qualitatively correct.

A comparison of pitot pressure obtained from RANS simulations and experiments for case 1 is shown in Fig. 7. The plane of data shown is at a distance of $x/d_{eff} = 8$. The extent of the data shown in the y and z directions are 0.0–7.0 and −4.0–4.0, respectively. The freestream flow is directed into the page. The numerical results are mirrored across the symmetry plane and the experimental data is overlaid on the numerical results for better comparison.

The wake is the bell-shaped structure centered around $z/d_{eff} =$ 0.0, near $y/d_{eff} = 0.0$. The wake region is characterized by low total pressures ($p_{02}/p_0 \sim 0.01$–0.03). The width of the wake region varies from $0.5z/d_{eff}$ to $2.0z/d_{eff}$ and the height of the wake region is approximately $1.8y/d_{eff}$. The boundary layer is thinner around the wake region. This is due to the action of the counter-rotating vortex pair capturing and lifting the surrounding boundary layer fluid. Comparing this with experimentally measured pitot pressure, it was found that the width of the wake region was approximately $1.25z/d_{eff}$. The height of the wake region was $1.8y/d_{eff}$, indicating that CFD predictions match experimental results. Boundary layer thinning around the wake is observed in experimental and numerical results. Above the wake region is the jet plume where the injectant fluid interacts with the freestream, forming a shear layer. The numerical prediction of the shear layer height matches the experimental value of $3.0y/d_{eff}$. Just beyond the shear layer is the inviscid region. The interaction shock wave is the last significant feature in Fig. 7. It is represented by the arch extending across the entire measurement plane with the peak located at $y/d_{eff} = 5.0$ and centered around $z/d_{eff} = 0.0$. Moving along the positive and negative z-axis direction, the height of the shock wave decreases and
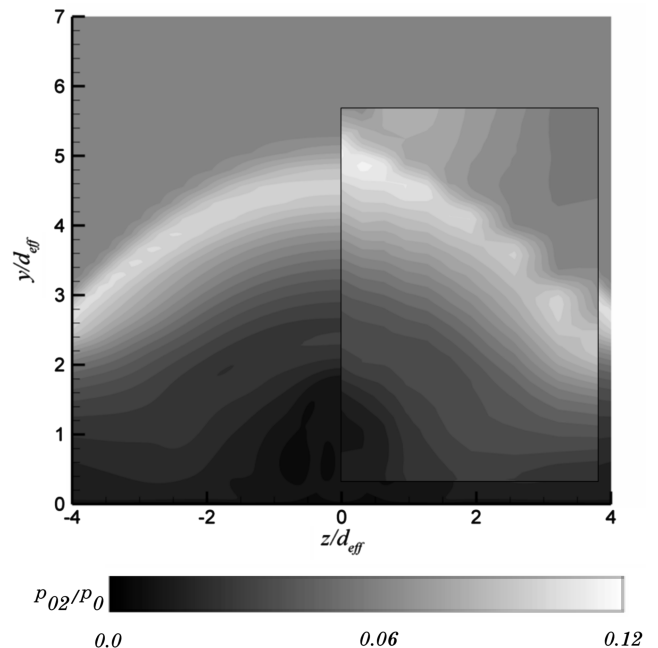

Fig. 7   Pitot pressure contours at $x/d_{eff} = +8.0$, case 1. The values are normalized by the freestream total pressure.
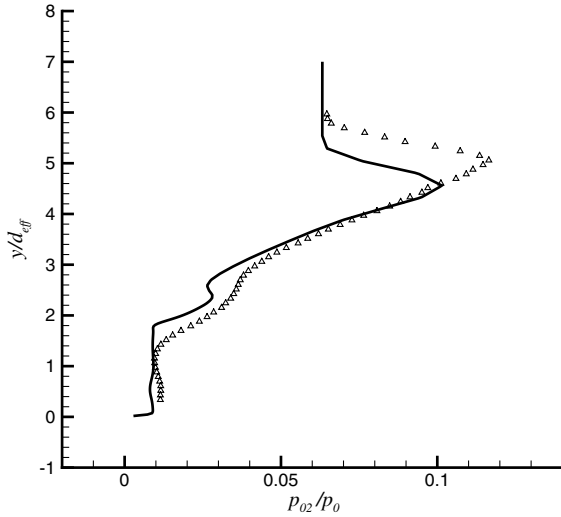
Fig. 8   Plot of pitot pressure at $z/d_{\text{eff}} = 0.0$ **and along the** y **axis. The line indicates numerical values and the symbols indicate experimental data.**
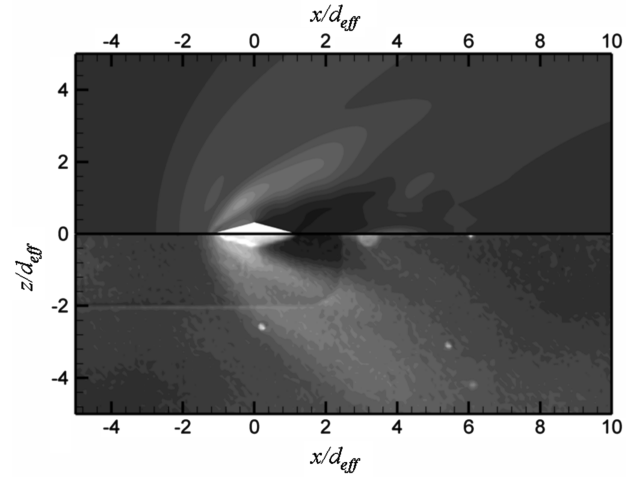

Fig. 9   Surface pressure comparison between experimental and numerical results, case 1. The top half of the image shows numerical results while the bottom half is experimental data. Refer to Fig. 10 for surface pressure contour levels.

at $z/d_{\text{eff}} = \pm 4.0$ it is $y/d_{\text{eff}} = 3.0$. The shock location was accurately predicted as compared to experimental results. Overall, the pitot pressure structure of the flowfield was captured with the CFD. However, the pressure in the wake region was underpredicted.

The ripples in the shock structure are artifacts produced during the experimental measurement. A five-hole probe was used in the experiments to measure the total and the static pressures. These values were then used to obtain the flow Mach number. The data were obtained along lines that were separated by 1/16th of an inch in the z direction. This leads to the formation of the ripple artifacts in the plots of experimental data and the CFD simulation is not expected to capture this phenomenon. The resolution in the y direction is much higher as the probe traverses in a continuous fashion.

A line plot of the pitot pressure along $z/d_{\text{eff}} = 0.0$ for both experimental and numerical data is shown in Fig. 8. Overall the agreement between the computation and experiment was considered good with the largest differences occurring near the interaction shock. The vertical extent of the shock was underpredicted by about 10%, which corresponds to about 3.0 mm or one probe diameter. The pitot pressure magnitude near the shock was underpredicted by about 20%. Assuming a conical shock wave, the observed difference corresponds to a local flow angle difference of approximately 2 deg, which indicates that the flow is sensitive to small errors in this region. In the wake and the plume regions, the predicted values follow the trend of the experimental results. The maximum deviation is about 10% in this region.

The wall pressure contour plots for case 1 are shown in Fig. 9. Wall pressures obtained from both experiments and CFD were normalized by the freestream pressure. The top half of the image is the result from CFD and the bottom half from the experiment. The freestream flow is from left to right in the image. Moving in the direction of the freestream flow, a slight increase ($\sim$1600 Pa) in pressure in the lambda shock region is seen in the CFD starting at about $x/d_{\text{eff}} = -2.0$ along the centerline. This small pressure increase was not observed in the experimental data, but is believed to be within the experimental scatter. Further downstream, the pressure rise was more substantial ($\sim 3.0 p/p_{\text{inf}}$), and overall the agreement between the CFD and experimental data in this region is considered good, where the CFD results were about 20% lower than the data. However, the surface topology is qualitatively correct. Around the trailing edge of the jet, the flow undergoes expansion leading to lower pressures ($\sim 0.4 p/p_{\text{inf}}$). This low-pressure region is observed in both the experiments and CFD. Again, the topology is qualitatively the same between the CFD results and experimental data.

In summary, the numerical results are converged. Furthermore, the agreement between the numerical solutions and the experimental data is sufficient to allow for flowfield conclusions to be drawn from the simulations.
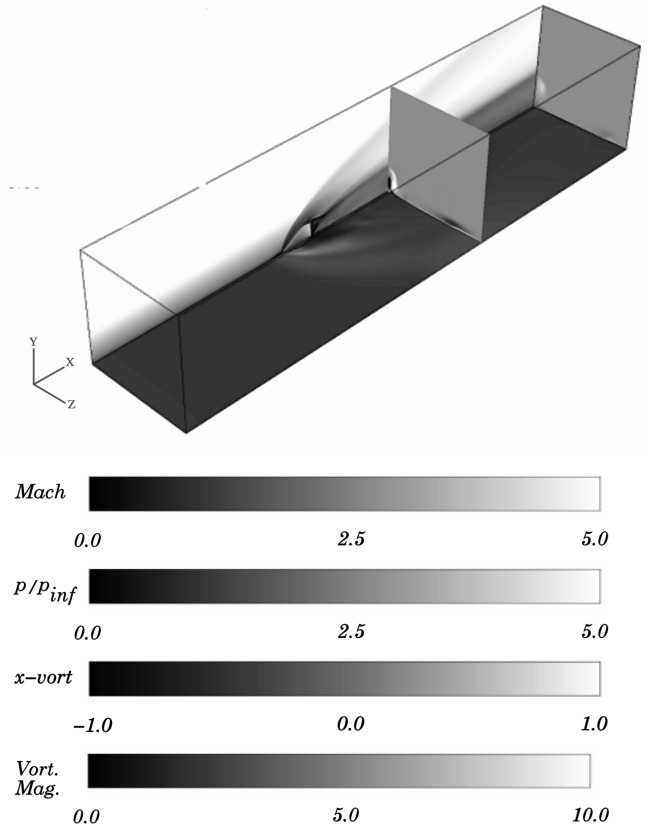
Fig. 10   Overall view of the diamond injector flowfield, case 1. The contours on the $x, y,$ **and** z **planes are that of** x **vorticity, surface pressure, and Mach number, respectively. The scales for the contours are also shown.**

IV.   Results and Discussion

A.   90 Deg Injection into a Mach 5.0 Freestream—Cases 1 and 2

1.   Flowfield Structure

An overview of the flowfield generated by normal injection through a diamond injector is shown in Fig. 10. The cross planes in the $x, y,$ and z Cartesian directions show contours of x vorticity, wall pressure, and Mach number, respectively. The freestream direction is along the x axis. Moving in the freestream direction, the first feature observed is the pressure rise on the tunnel floor due to the presence of
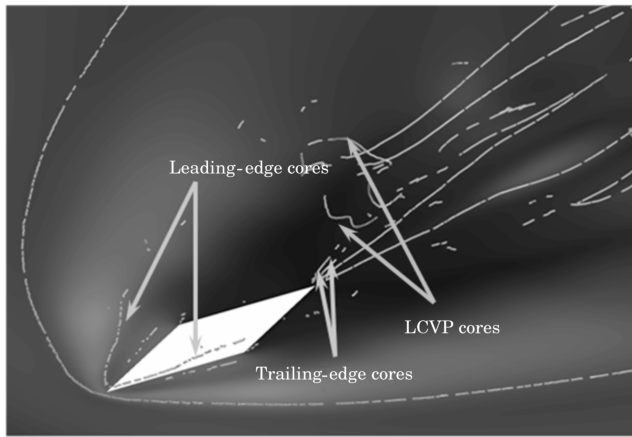
Fig. 11   Leading- and trailing-edge vortex cores, case 1. Refer to Fig. 10 for surface pressure contour levels.
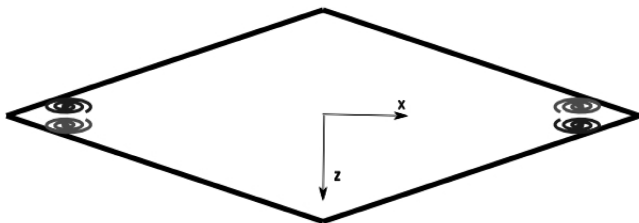

Fig. 12   Illustration of injector boundary layer vortices.

a lambda shock as discussed in the Introduction. The interaction shock can be clearly seen in the Mach number plot on the z plane. Immediately downstream of the interaction shock, the barrel shock structure outline is observed. Significant pressure rise occurs around the front half of the injector due to the interaction between the injector and the freestream boundary layer fluid. A low-pressure and low Mach number region is observed downstream of the injector port. The axial counter-rotating vortex pair can be seen on the x plane with contours of x vorticity. Away from the centerline of the tunnel, the vorticity due to the horseshoe vortex can also be observed. The shear layer formed due to the interaction between the freestream and injector fluid is clearly seen downstream of the injector, on the z plane.

For the most part, the overall structure is similar to that of a circular injector. However, the diamond shape introduces two new vortex features, which are described in more detail in the following subsections.

2.   Corner Vorticity

The diamond injector shape introduces two new pairs of vortices at the leading and trailing edges of the injector. The vortex cores associated with these new vortices are shown in Fig. 11. The formation of these vortices is attributed to the corner flow vorticity production in the boundary layer within the injector port at the leading and trailing edges. This is illustrated in Fig. 12. The two leading-edge vortices undergo lateral separation as the injector fluid travels downstream. This is due to the expansion of the injector fluid in the lateral direction. The maximum separation between the vortices occurs close to the trailing edge of the injector port and is approximately $2.0d_{eff}$. The two trailing-edge vortices feed into yet another new feature described in the next section.

The interaction between the freestream boundary layer fluid and the injector fluid may also be a contributing factor for the formation of the leading-edge vortex pair. It is observed that this vortex pair entrains fluid from the outer regions of the freestream boundary layer (i.e., the region away from the wall) as well as from the injector as shown in Fig. 13. Thus, this vortex pair could induce enhanced mixing of freestream and injector fluids. As will be seen in a later
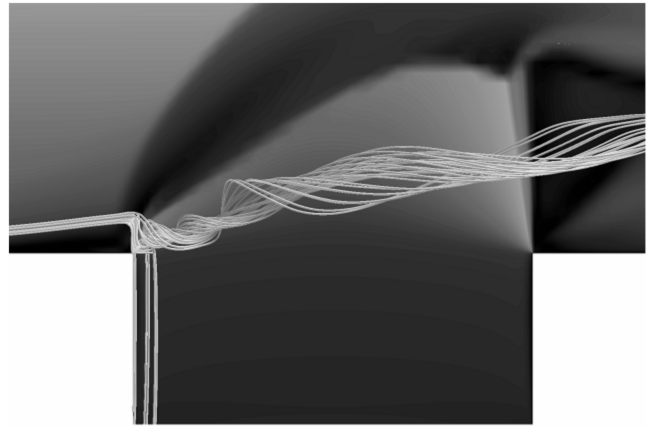

Fig. 13   Mixing of injector and boundary layer fluid, case 1. Refer to Fig. 10 for Mach number contour levels.

section, sweeping the injector port leading-edge angle (α) enhances this vortex production mechanism.

3.   Lateral Counter-Rotating Vortex Pair (LCVP)

A second new vortex pair has been identified in this flow above the floor immediately downstream of the barrel shock. The axes of this vortex pair are oriented in the z-axis direction. The cores of this vortex pair are shown in Fig. 11. This new structure is particularly interesting because it has the potential to serve as a gasdynamically induced flame holder. What follows is an attempt to explain the formation of this structure.

After analyzing the flow structures in detail, it was found that the LCVP formation is closely coupled with the barrel shock shape. The shape of the barrel shock was significantly different for the diamond injector configuration as compared to that generated by a circular orifice [20]. The surface of the barrel shock was visualized using the isosurface of entropy that was clipped based on the y component of velocity. The barrel shock structure generated by the case 1 injector is shown in Fig. 14. The barrel shock had a sharp leading edge. The width of the shock surface was proportional to the height above the floor. The shock was found to expand more in the lateral direction
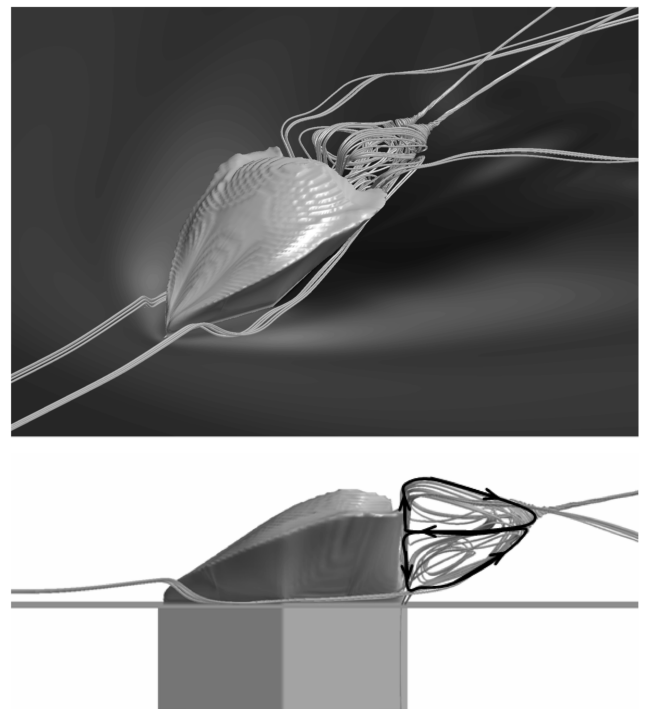

Fig. 14   Structure of LCVP, case 1. Refer to Fig. 10 for surface pressure contour levels.

than in the axial direction due to the axis reversal [13] phenomenon. The Mach disk surface was not as prominent as in a circular injector case. The trailing edge of the barrel shock for case 1 was a surface normal to the freestream direction as indicated in Fig. 14. The formation of this shock surface is analogous to a Japanese "sensu" fan, that is, the shock expanded in the lateral direction as the fluid exited the injector port and formed a shape similar to the shape of the nabla symbol. The streamlined forebody coupled with the nabla-shaped trailing edge facilitated the formation of the LCVP. The low pressures generated on the downstream side of the barrel shock caused part of the incoming freestream boundary layer fluid to lift off the tunnel floor. This fluid interacted with the injector fluid, which was turning in the freestream direction. A recirculating flow was set into motion due to this interaction. This recirculation region contained a pair of vortices with axes in the z direction. The top vortex rotated in the clockwise direction and the bottom vortex in the counterclockwise direction forming an "8"-shaped structure as observed from the positive z axis. The structure of this vortex pair is shown in Fig. 14.

Further analysis of this vortex pair reveals interesting features. A pair of cone-shaped structures were formed at the downstream edge of this vortex pair. This is displayed in Fig. 15. Part of the fluid rotating in the top vortex was captured in the cone-shaped structures. At the tip of these cones, the fluid separated into components (see inset in Fig. 15). One of the components was ejected in the downstream direction while the other component was ejected upstream. The component that was ejected upstream was engulfed by the top vortex. Another ejection mechanism was the capture and transport of fluid in the LCVP by the axial CVP as it moved past the barrel shock. This is shown in Fig. 16.
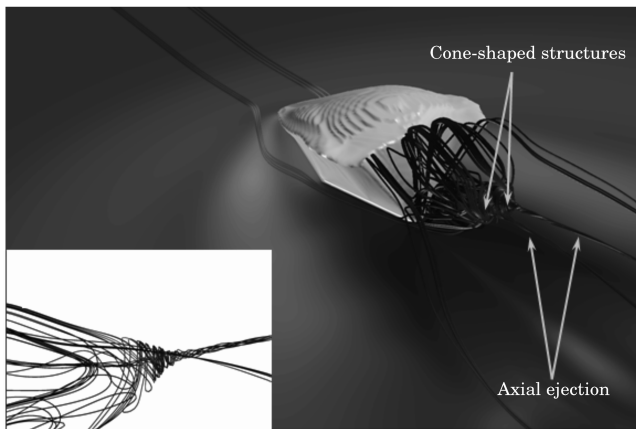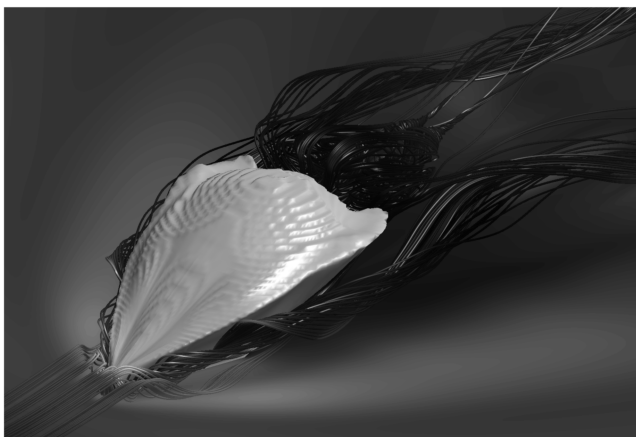
It was observed that the LCVP entrained the injector trailing-edge vortex pair (mentioned in the previous section) fluid. Thus, a potential application for the LCVP vortex pair is a gasdynamically induced flame holder in a scramjet combustor. The potential advantages of using this structure for flame holding as compared to cavity flame holders include reduced heat transfer to the wall (because the vortices are not in contact with the wall) and elimination of instabilities induced into the flow due to the presence of cavities. Another important requirement for this structure to act as a flame holder is the residence time of the fluid passing through this vortex pair. It was found that the residence time of the streamlines passing through the LCVP was about 10 times that of the residence time of the freestream streamlines.

Because the LCVP has not been previously reported, a study was performed to verify that this structure was independent of the CFD code and turbulence model. Thus, a turbulence model parametric study was performed with GASP. The turbulence models included Spalart–Allmaras [21] one-equation mode, k–ω [16], and Menter's shear stress transport (SST) [22] with and without compressibility corrections. In addition, Menter's SST and SST-DES (detached eddy simulation) simulations were performed with the unstructured code Cobalt [23]. A detailed description of these simulations is given in Srinivasan and Bowersox [20] and Srinivasan [24]. In summary, the secondary flow structure including the LCVP structure shown in Fig. 14 was essentially the same in all of the simulations including the instantaneous and time-averaged DES shown in Fig. 17. Because the flow structure was found to be independent of the code and turbulence model, the GASP code was selected for the present flowfield parametric study because of numerical efficiency and easier visualization of the solution on structured grids.

The magnitude of vorticity on the centerplane of the domain and a crossplane at $x/d_{eff} = 8.0$ is shown in Fig. 18. The magnitudes of the LCVP and CVP were found to be of the same order. The wake vortices that are generated in transverse jet injection flows are also observed in the vorticity plot on the crossplane. It was found the wake vortices do not interact with the LCVP structure. The flowfield results were subjected to further postprocessing to obtain the relative

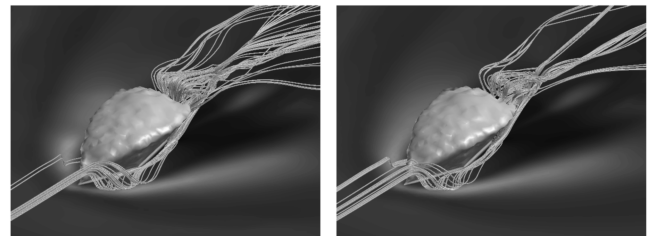Fig. 15   Cone-shaped structures downstream of LCVP, case 1. Refer to Fig. 10 for surface pressure contour levels.

a) Instantaneous   b) Time averaged

Fig. 17   Detached eddy simulation results, case 1.

Fig. 16   Lateral ejection mechanism, case 1. Refer to Fig. 10 for surface pressure contour levels.
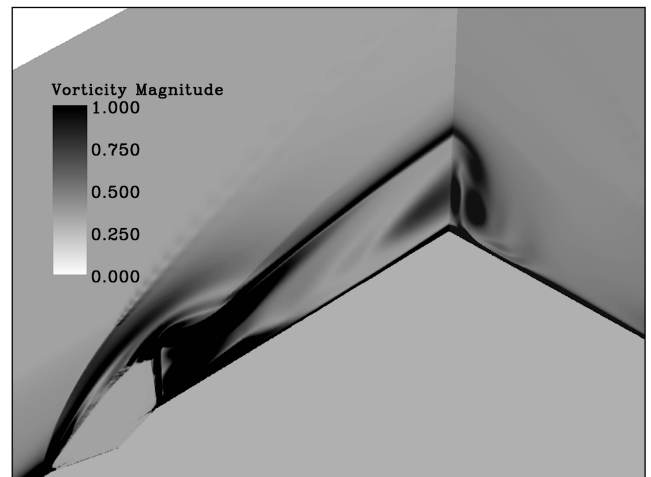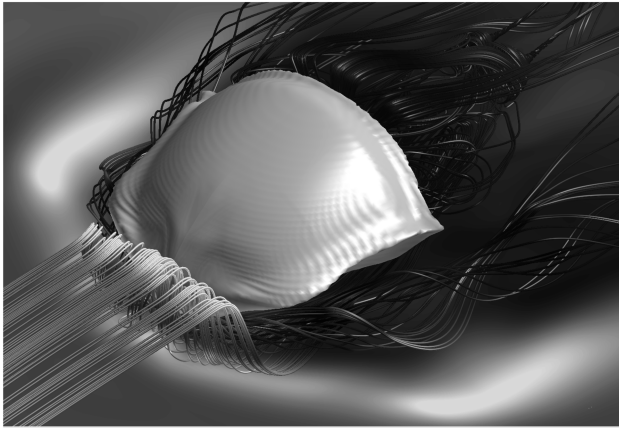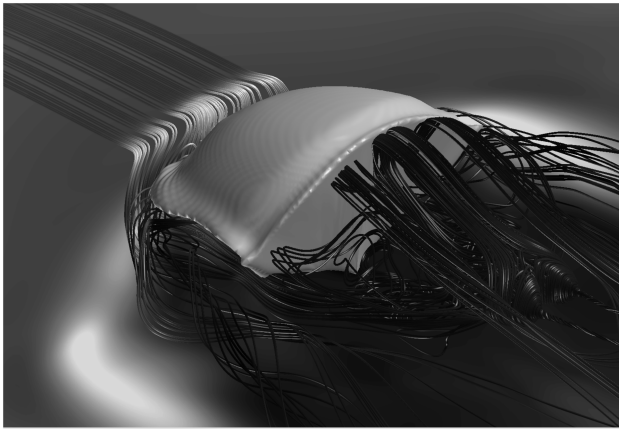

Fig. 18   Contours of vorticity magnitude, case 1.

a)

b)

Fig. 19 Barrel shock and LCVP in normal injection, case 2. Refer to Fig. 10 for surface pressure contour levels.

a)

b)

Fig. 20 Vortex cores and vorticity magnitude of leading-edge vortices, case 3. Refer to Fig. 10 for surface pressure and vorticity magnitude contour levels.
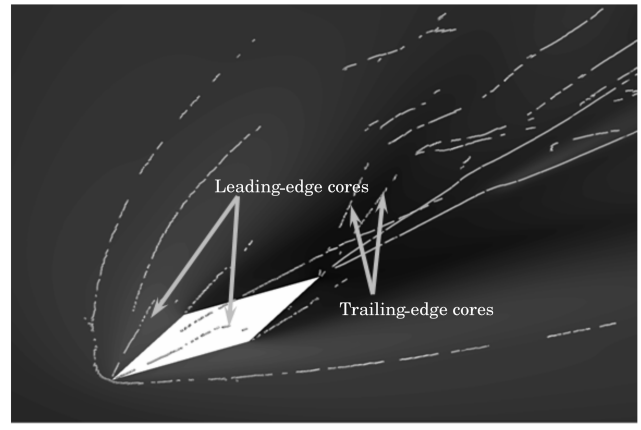
magnitude of terms in the compressible vorticity transport equation. The results from this analysis suggest that the most significant terms are those of compressibility and vortex stretching whereas the viscous terms contribute the least to the formation of the LCVP. Thus, the formation of the LCVP seems to be a primarily inviscid phenomenon. Additional details of the vorticity transport analysis are provided by Srinivasan [24].

The higher pressure injection case (case 2) demonstrated a marked change in the shape of the barrel shock. The fan angle of the nabla-shaped surface at the trailing edge was larger, leading to a change in the LCVP structure near the tunnel floor (see Fig. 19). The LCVP, though present, was significantly altered in this case. Specifically, the axial extent of the upper vortex was larger. The lower vortex was more three dimensional and chaotic because spanwise edges of the barrel shock trailing surface were closer to the floor. This inhibited the freestream boundary layer fluid from flowing into this region. The cone-shaped ejection vortices seen in case 1 were also formed in this case, as illustrated in Fig. 19.
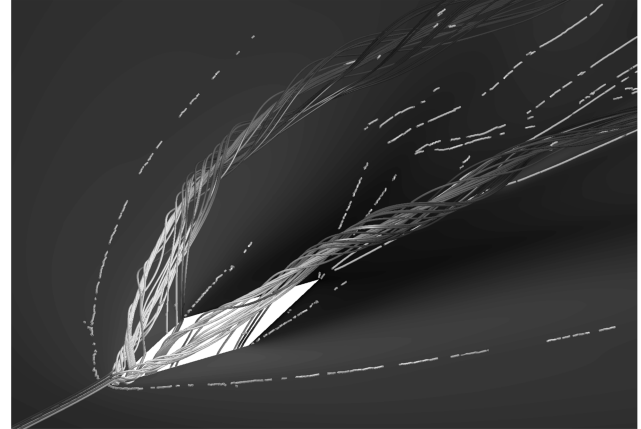
In addition to these two cases (cases 8 and 9, not shown), simulations for 10-deg and 20-deg injector half-angles at the lower pressure condition were also performed for the Mach 5.0 freestream condition. For the 10-deg case, the barrel shock was streamlined in the lateral direction from the leading edge to the trailing edge. For the 20-deg case, the upper surface of the barrel shock was sloped near the trailing edge. Hence, the nabla-shaped shock shape at the trailing edge was absent for both. The LCVP was not observed for either of these half-angles, which reinforces the idea that the formation of this vortex structure couples to the barrel shock shape.

B. Angled Injection into a Mach 5.0 Freestream—Case 3

Simulations were also performed with angled injectors. Overall, the flowfield was similar to the 90-deg injection, with some notable differences. As an example, results from case 3 (45-deg angled injection) are presented in Fig. 20. For this case, higher vorticity levels were observed in the injector leading-edge region, indicating that mixing is stronger as compared to case 1. Both lateral and normal penetrations of these cores were also found to be larger at downstream locations. It was observed that injector fluid streamlines from further downstream of the injector leading edge were also incorporated into the leading-edge mixing mechanism. The normalized values of the magnitude of vorticity are indicated on the vortices as seen in Fig. 20. The vorticity levels drop significantly by the time the lateral separation between the vortices reaches a maximum near the injector trailing edge. The 27.5-deg simulation results (case 10, not shown) exhibited strong similarities to the 45-deg injection simulations.

The LCVP structure was not observed in the angled injection simulations. This was because the trailing edge of the barrel shock was swept in the downstream direction, which aligned the boundary layer fluid in this region into the flow direction.

C. Hybrid Injection into a Mach 5.0 Freestream—Cases 4 and 5

In an effort to produce an injector with enhanced leading-edge mixing while maintaining the LCVP structure, two hybrid configurations were investigated (see Fig. 2). These are denoted by case 4 and case 5 in Table 2.

The shape of the barrel shock was the determining factor in the formation of the LCVP structure in case 1. To maintain the shape of the barrel shock at the trailing edge, the injector trailing-edge angle (β) of the injectors was maintained at 90 deg. The leading-edge angles (α) for the two hybrid cases were 45 and 27.5 deg, respective to the freestream direction. The shape of the barrel shocks obtained from these simulations, as shown in Figs. 21 and 22, indicates a
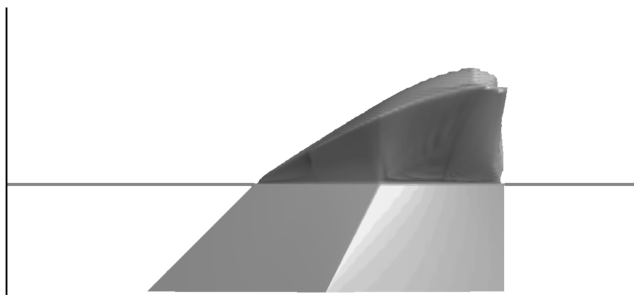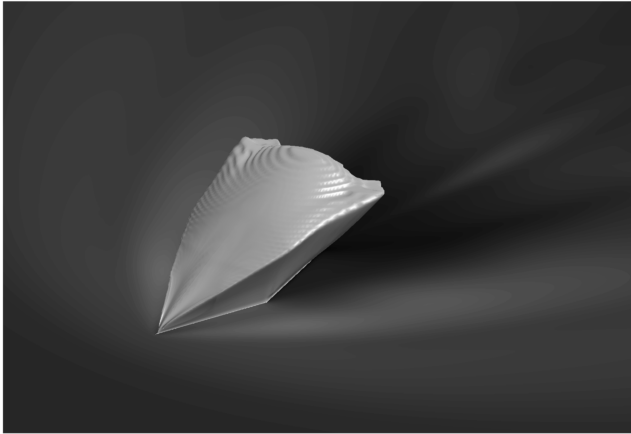
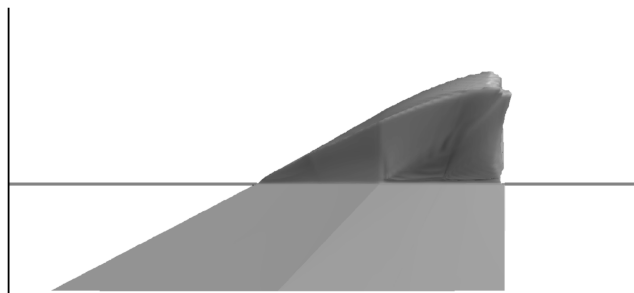Fig. 21   Barrel shock structure, case 4. Refer to Fig. 10 for surface pressure contour levels.
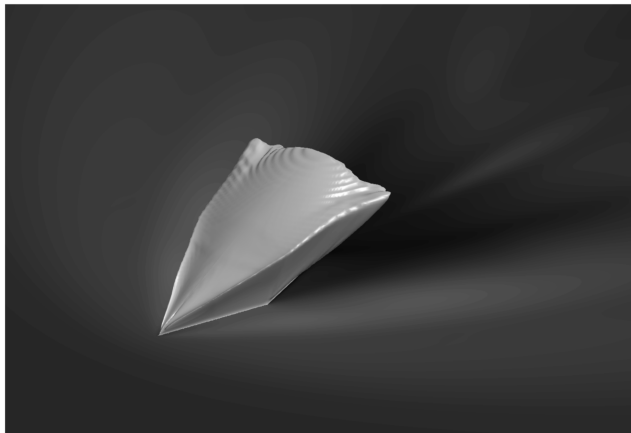

Fig. 22   Barrel shock structure, case 5. Refer to Fig. 10 for surface pressure contour levels.
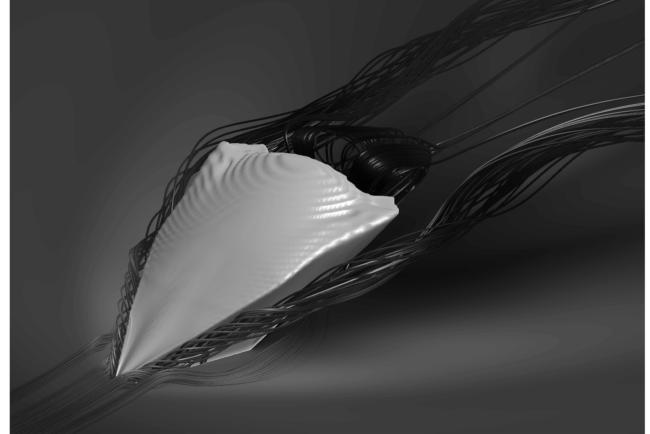

Fig. 23   Leading-edge and LC vortex pair, case 4. Refer to Fig. 10 for surface pressure contour levels.
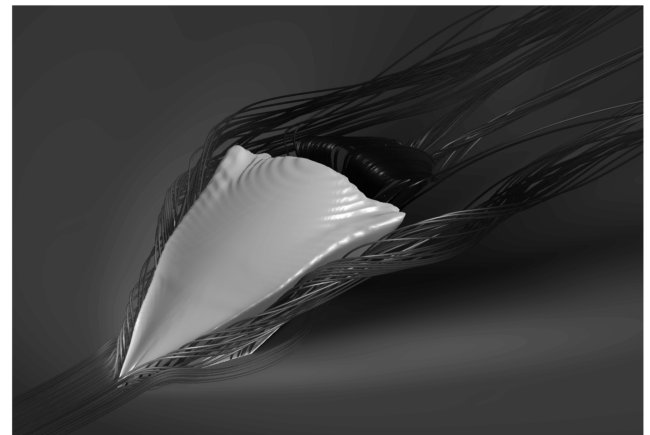

Fig. 24   Leading-edge and LC vortex pair, case 5. Refer to Fig. 10 for surface pressure contour levels.

The LCVP structure was observed in both hybrid injector simulations and can be seen in Figs. 23 and 24. The structure is similar to the one found in case 1. The cone-shaped structures at the trailing edge of the LCVP can also be seen in the figure.

The leading-edge mixing vortex was stronger than case 1 but not as strong as that seen in case 3. This suggests that the enhanced leading-edge mixing mechanism shown in case 3 was in part due to the downstream sweep and associated shock shape. Also, because the velocity vectors of injector fluid at the leading edge of the injector have inclinations larger than the corresponding injector inclination, the vorticity at the leading edge is lower as compared to case 3. However, the vortices exist and contribute to the mixing of freestream and injector fluid. It was observed that the pressure rise across the interaction shock was lower in the hybrid injection cases as compared to the normal injection case. This indicates a weaker shock and leads to lower drag.

D.   90 Deg Injection into a Mach 2.0 Freestream—Cases 6 and 7

Additional simulations were performed to investigate the effect of freestream Mach number on the newly identified diamond port induced LCVP flow structure. The freestream conditions were identical to that of the Mach 5.0 cases except for the change in Mach number. The conditions are listed in Tables 1 and 2. Two different injector half-angles (γ) of 15 and 10 deg were used in these simulations.

Results obtained in case 6 showed that the shape of the barrel shock (see Fig. 25) was similar to that seen in case 1, with the only difference being the height of the shock. The trailing-edge surface of the shock was perpendicular to the freestream flow. With the change
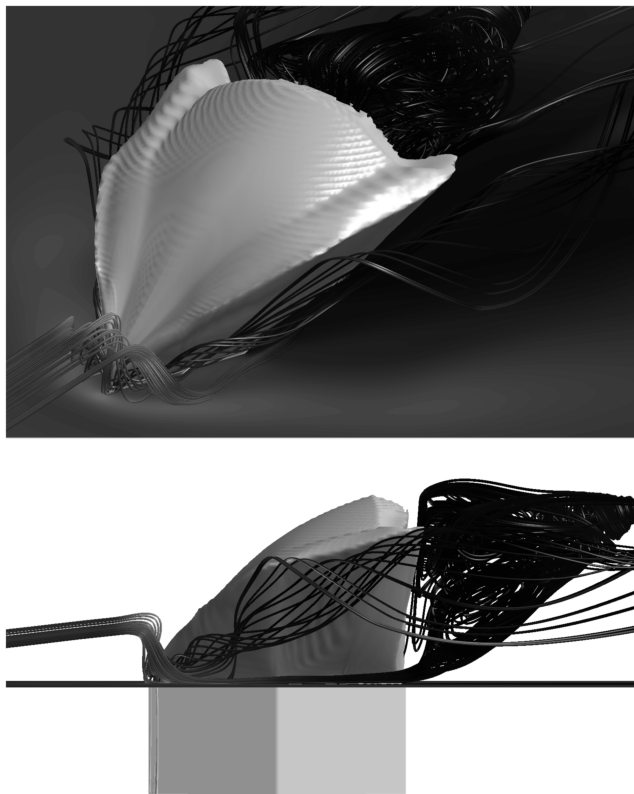
structure very similar to the normal injection case. The one notable difference is the inclination of the shock surface at the leading edge. As expected, it was found that the shock leading-edge angle was proportional to α. For both hybrid injectors, the trailing edge of the barrel shock exhibited the same nabla-shaped surface seen in case 1.

Fig. 25 LCVP structure, case 6. Refer to Fig. 10 for surface pressure contour levels.
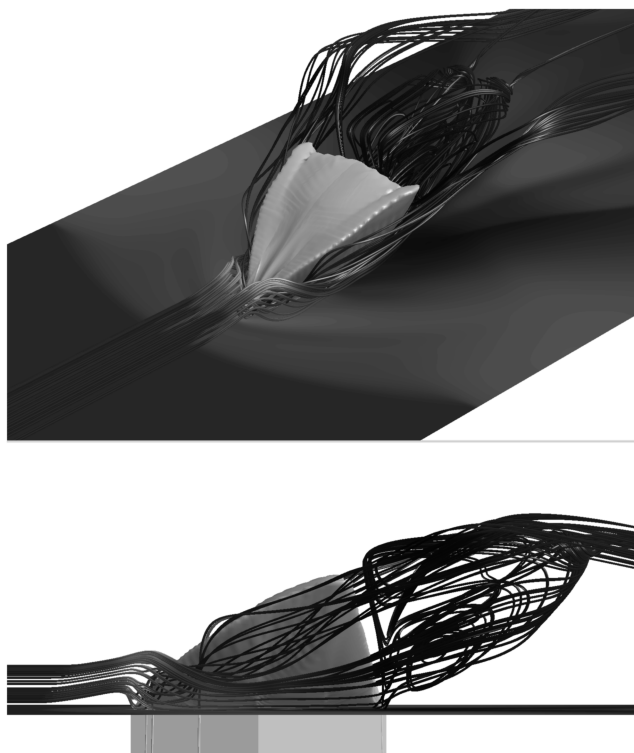

Fig. 26 LCVP structure, case 7. Refer to Fig. 10 for surface pressure contour levels.

in the injector half-angle (case 7), it was observed that the barrel shock shape, shown in Fig. 26, was again similar to case 1. The height of the shock was found to be comparable to that in case 6. However, the trailing-edge surface was inclined in the upstream direction.

The shape of the barrel shock created favorable conditions for the formation of the LCVP vortex pair in cases 6 and 7 (see Figs. 25 and 26). This is similar to the flowfield analyzed in case 1. The transverse and axial extents of the LCVP were seen to scale with the height of the barrel shock as shown in Fig. 25. The inclined trailing-edge surface of the shock led to the inclination of the LCVP structure as seen in Fig. 26. The cone-shaped structures, formed in case 1, near the downstream region of the LCVP were also observed in cases 6 and 7

V. Conclusions

Numerical simulations were performed to study the effects of the barrel shock, induced by transverse underexpanded sonic injection through diamond-shaped orifices, on near-field secondary flow structures in a supersonic ($M = 2$ and 5) crossflow. The GASP flow solver was used to execute these simulations.

Results from the normal injection case were analyzed to obtain an overall characterization of the flow structure. Two new vortex features were observed in the vicinity of the injector port. First, a pair of vortices were formed near the leading edge of the injector due to the corner vortices in the injector port and the interaction between the freestream and injector fluids. This leading-edge vortex pair has the potential to serve as a mixing enhancement mechanism. Second, it was found that the shape of the barrel shock generated by the diamond-shaped injector tailored the flow around the injector port leading to the formation of a vortex pair downstream of the injector port. This gasdynamically induced flow structure, termed the lateral counter-rotating vortex pair, has the potential to act as a flame-holding device (a tenfold increase in residence time was observed). A series of simulations were performed to characterize the controllability of the two new flow structures. The specific findings are listed below.

At Mach 5.0, the presence of the LCVP was found to depend strongly on the injector half-angle. Specifically, the LCVP was present at 15 deg but not at 10 or 20 deg. It was also observed that the LCVP did not form in simulations of angled transverse injection, whereas, the leading-edge vortex pair was found to be stronger as compared to normal injection. Simulations were performed using hybrid injectors with angles $\alpha - \beta$ of 45–90 deg and 27.5–90 deg to combine the advantages of the leading-edge mixing and the LCVP structure. The LCVP structure was observed in both of these simulations. The leading-edge vorticity (mixing) was found to be enhanced as compared to the normal injection case. Simulations were also performed at a different freestream condition with lower Mach number (Mach 2.0) and two different injector half-angles of 15 and 10 deg. The shape of the barrel shocks was similar to that of the normal injection simulation and the LCVP structure was also observed in both of these cases. The LCVP was found to scale with the height of the barrel shock.

References

[1] Heiser, W., and Pratt, D., *Hypersonic Airbreathing Propulsion*, AIAA Education Series, AIAA, Washington, D.C., 1994.

[2] Davis, D. L., and Bowersox, R. D. W., "Stirred Reactor Analysis of Cavity Flame Holders for Scramjets," AIAA Paper 1997-3274, July 1997.

[3] Davis, D. L., and Bowersox, R. D. W., "Computational Fluid Dynamics Analysis of Cavity Flame Holders for Scramjets," AIAA Paper 1997-3270, July 1997.

[4]   Srivastava, B., "Aerodynamic Performance of Supersonic Missile Body- and Wing Tip-Mounted Lateral Jets," *Journal of Spacecraft and Rockets*, Vol. 35, No. 3, 1998, pp. 278–286.

[5]   Brandeis, J., and Gill, J., "Experimental Investigation of Super- and Hypersonic Jet Interaction on Missile Configurations," *Journal of Spacecraft and Rockets*, Vol. 35, No. 3, 1998, pp. 296–302.

[6]   Chamberlain, R., McClure, D., and Dang, A., "CFD Analysis of Lateral Jet Interaction Phenomenon for the THAAD Interceptor," *38th AIAA Aerospace Sciences Meeting and Exhibit*, AIAA, Reston, VA, Jan. 2000.

[7]   Zukowski, E., and Spaid, F., "Secondary Injection of Gases into a Supersonic Flow," *AIAA Journal*, Vol. 2, No. 10, 1964, pp. 1697–1705.

[8]   Schetz, J., and Billig, F., "Penetration of Gaseous Jets Injected into a Supersonic Stream," *Journal of Spacecraft and Rockets*, Vol. 35, No. 11, 1966, pp. 1658–1665.

[9]   Chenault, L., Beran, P., and Bowersox, R., "Numerical Investigation of Supersonic Injection Using a Reynolds-Stress Turbulence Model," *AIAA Journal*, Vol. 37, No. 10, 1999, pp. 1257–1269.

[10] McClinton, C., "The Effects of Injection Angle on the Interaction Between Sonic Secondary Jets and as Supersonic Freestream," NASA TR TN D-6669, 1972.

[11] Barber, M., Schetz, J., and Roe, L., "Normal Sonic Helium Injection Thorough a Wedge Shaped Orifice into a Supersonic Flow," *Journal of Propulsion and Power*, Vol. 13, No. 2, 1997, pp. 257–263.

[12] Bowersox, R., Fan, H., and Lee, D., "Sonic Injection into a Mach 5.0 Freestream Through Diamond Orifices," *Journal of Propulsion and Power*, Vol. 20, No. 2, 2004, pp. 280–287.

[13] Tomioka, S., Jacobsen, L., and Schetz, J., "Sonic Injection from Diamond-Shaped Orifices into a Supersonic Flow," *Journal of Propulsion and Power*, Vol. 19, No. 1, Jan.–Feb. 2003, pp. 104–114.

[14] GASP Ver. 4.0 Users' Manual, AeroSoft, Inc., Blacksburg, VA, 2001.

[15] Neel, R. E., Godfrey, A. G., and Slack, D. C., "Turbulence Model Validation in GASP Version 4," AIAA Paper 2003-3740, 2003.

[16] Wilcox, D. C., *Turbulence Modeling for CFD*, DCW Industries, Inc., La Canada, CA, 1998.

[17] Roe, P. L., "Approximate Riemann Solvers, Parameter Vector, and Difference Schemes," *Journal of Computational Physics*, Vol. 43, No. 2, 1981, pp. 357–372.

[18] Harten, A., and Hyman, J. M., "Self Adjusting Grid Methods for One-Dimensional Hyperbolic Conservation Laws," *Journal of Computational Physics*, Vol. 50, No. 2, 1983, pp. 235–269.

[19] Hirsch, C., *Numerical Computation of Internal and External Flows, Volumes 1 and 2*, Wiley, New York, 1992.

[20] Srinivasan, R., and Bowersox, R., "Role of the Barrel Shock as Control Element for Hypersonic Transverse Jet Injection Flows," AIAA Paper 2004-2698, 2004.

[21] Spalart, P. R., and Allmaras, S. R., "A One Equation Turbulence Model for Aerodynamic Flows," *La Recherche Aerospatiale*, Vol. 1, 1994, pp. 5–21.

[22] Menter, F., "Two-Equation Eddy-Viscosity Turbulence Models for Engineering Applications," *AIAA Journal*, Vol. 32, No. 8, 1994, pp. 1598–1605.

[23] Strang, W. Z., Tomaro, R. F., and Grismer, M. J., "The Defining Methods of Cobalt60: A Parallel, Implicit, Unstructured Euler/Navier-Stokes Flow Solver," AIAA Paper 1999-0786, Jan. 1999.

[24] Srinivasan, R., "Improved Understanding and Control of High-Speed Jet Interaction Flows," Ph.D. Thesis, Texas A&M University, College Station, TX, 2005.